

Robust Detection of Infrared Maritime Targets for Autonomous Navigation

Bin Wang, Emrah Benli, *IEEE Member*, Yuichi Motai*, *IEEE Senior Member*, Lili Dong and Wenhai Xu

Abstract—This paper addresses a problem on infrared maritime target detection robustly in various situations. Its main contribution is to improve the infrared maritime target detection accuracy in different backgrounds, for various targets, using multiple infrared wave bands. The accuracy and the computational time of traditional infrared maritime searching systems are improved by our proposed Local Peak Singularity Measurement (LPSM)-Based Image Enhancement and Grayscale Distribution Curve Shift Binarization (GDCSB)-Based Target Segmentation. The first part uses LPSM to quantize the local singularity of each peak. Additionally, an enhancement map (EM) is generated based on the quantitative local singularity. After multiplying the original image by the EM, targets can be enhanced and the background will be suppressed. The second part of GDCSB-Based Target Segmentation calculates the desired threshold by cyclic shift of the grayscale distribution curve (GDC) of the enhanced image. After binarizing the enhanced image, real targets can be segmented from the image background. To verify the proposed algorithm, experiments based on 13,625 infrared maritime images and five comparison algorithms were conducted. Results show that the proposed algorithm has solid performance in strong and weak background clutters, different wave bands, different maritime targets, etc.

Index Terms—Infrared imaging, image segmentation, maritime surveillance, target detection.

I. INTRODUCTION

The robust infrared maritime target detection has been a research hotspot for recent decades to improve the performance of infrared maritime searching system's performance [1-3]. Compared with traditional thermal or multi-spectral target detection [4, 5] or tracking [6] technology, infrared maritime target detection is different because: 1) Fewer feature sources (color, texture, shape, motion pattern, etc.) to exploit; 2) The

image background would typically be wavy, periodical and frequently changing, but contaminated by fewer types of interference; 3) A target can be periodically overwhelmed by clutters; 4) No prior knowledge would be available for maritime search or surveillance. Thus, it is difficult to detect various infrared maritime targets accurately in a single frame by traditional target detection or tracking algorithms.

Algorithms for infrared maritime target detection can be basically classified into two categories: Track-before-Detect and Detect-before-Track (DBT). Track-before-Detect, like the particle filter [7-9], typically keeps updating the status of each observation model for every suspected target using the accumulated information from image sequences and some prior knowledge [10, 11]. This is highly time-consuming and complex in computation, leading to a low applicability in real maritime missions. By contrast, DBT focuses on extracting targets based on information from a single infrared maritime image, which is more efficient and application-friendly [12].

However, when there are strong ocean waves, these existing DBT algorithms cannot suppress the background wave clutters well enough to guarantee a low false alarm rate (FAR) while keeping the missing alarm rate (MAR) at 0. In addition, when both strong and weak targets show up simultaneously, traditional algorithms would typically miss weak targets. Thus, it is still a great challenge and significant task to develop a robust single-image detection algorithm in these situations. Our proposed algorithm achieved this challenge by searching the local maximum targets throughout a single image. This process overcomes the loss of weak targets problem in the entire image.

Ocean waves typically have a periodic motion pattern on the sea surface [13, 14]. Thus, the intensity distribution of ocean wave clutters in an infrared maritime image would also be periodic. That is to say that one ocean wave clutter could always find its counterparts in a neighbor area. On the contrary, the target is singular in the local area in terms of the intensity distribution. Due to this condition, it is reasonable to suppress background clutters through reducing the intensity of pixels which have low intensity singularity and high intensity similarity in the neighboring areas. The fast binarization could, then, be adopted to segment the real targets. Based on these analyses, this paper comes up with a robust single-frame detection algorithm for infrared maritime targets in strong ocean waves. It consists of the image enhancement by the **Local Peak Singularity Measurement (LPSM)** and the target segmentation by the **Grayscale Distribution Curve Shift Binarization (GDCSB)**. Strong ocean waves are filtered by using the singularity of the target in its local pixel neighborhood and LPSM helps to distinguish the waves and the

B. Wang is with the Electronic and Computer Engineering department, School of Engineering, Virginia Commonwealth University, Richmond, VA, USA, and also with the Information and Communication Engineering department, School of Information Science and Technology, Dalian Maritime University, Dalian, China (e-mail: dmluwb@126.com).

E. Benli is with the Department of Electrical and Electronics Engineering, Gümüşhane University, Gümüşhane, 29100 Turkey (e-mail: benlie@vcu.edu).

Y. Motai is with the Electronic and Computer Engineering department, School of Engineering, Virginia Commonwealth University, Richmond, VA, USA (e-mail: ymotai@vcu.edu).

L. Dong and W. Xu are with the Information and Communication Engineering department, School of Information Science and Technology, Dalian Maritime University, Dalian, China.

targets in the corresponding area. The proposed algorithm achieves this by eliminating the time-consuming problem of Track-before-Detect process. Our algorithm speeds-up the detection process as in DBT while increasing the accuracy of filtering the ocean wave noise.

Compared with existing algorithms, the nature of the wave’s periodic motion pattern was highly exploited in our proposed algorithm. Relying on the wave’s local similarity and the target’s local singularity in intensity and contrast, the background clutter was effectively suppressed and targets were enhanced at the same time. In particular, our proposed algorithm could narrow the saliency gap between strong and weak targets and guarantee a high possibility of discovering strong and weak targets simultaneously.

Experiments and systematic data analyses in Sec. VI would demonstrate that, compared with existing DBT algorithms, our proposed strategy can perform much better on single-image infrared maritime target detection for different targets, under various environment conditions and using multiple infrared wave bands. Specifically, in some challenging scenarios, like strong ocean waves or both strong and weak targets show up, the proposed algorithm could outperform existing algorithms.

II. RELEVANT STUDIES OF DBT FOR INFRARED MARITIME TARGET DETECTION

Recent years have seen many DBT algorithms that work on this issue. Table I lists six state-of-the-art categories of these DBT algorithms and some representative papers for each category.

Among these categories, the **Visual Attention Mechanism** has drawn the most interest in recent years. This mechanism simulates the working principles of the human visual system and can generate similar detection results as observed in human eyes [15]. The Difference of Gaussian filters and their improved versions [16, 17] have the most similar performance to the contrast mechanism of human visual systems. The local self-similarity and local contrast of an image were also used to generate the contrast saliency map [18]. Boolean map visual theory [19] can also work in the contrast mechanism. Meanwhile, the visual attention model was used to infer scenario background to perform accurate background subtraction and target segmentation [17]. In addition, the pulsed discrete cosine transform was combined with Gaussian filtering to generate saliency maps [20], followed by adaptively fusing saliency maps from different transformation bases.

TABLE I
SIX STATE-OF-THE-ART DBT CATEGORIES FOR INFRARED MARITIME TARGET DETECTION

DBT Category	Representative References
Visual Attention Mechanism	[15-20]
Transformation Domain	[2, 21-26]
Morphology	[12, 27-29]
Region Characteristics	[11, 30-33]
Sparse Representation	[34-39]
Pixel Characteristic Analysis	[40-42, 46]

The **Transformation Domain**, like wavelet transformation, is superior in multiresolution and multidirection analysis so that

it is a popular technique for infrared maritime target detection. In terms of wavelet transform, the strong inter-subband correlation of targets could contribute to the accurate detection for maritime targets [2], even when there was heavy sea fog [21]. The wavelet transform combined with the probability density functions of the wavelet subband also helped segment real targets from background clutters [22]. Apart from these, the tailored wavelet model [23], wavelet-based background construction [24], etc. were also used in infrared maritime target detection. In [25], original images were transformed into the infrared gradient vector field, where background clutter had strong direction coherence and targets did not. This feature gap was utilized to distinguish targets from background clutter. Besides, different band-limited subsignals were used in [26] to analyze image feature in frequency domain. After threshold segmentation in certain subsignals, targets could be detected.

Background clutters suppression can be implemented with **Morphology**. For example, the morphological anisotropic diffusion filtering was proposed to predict the incoming background information [27], which was subtracted from the original image. Besides, the multi-scale operation of a new top-hat transformation [12], top-hat transformation integrated with the second prediction difference [28], etc. were proposed to enhance the performance of infrared maritime target detection. In [29], an improved TOP-HAT filter, cooperated with open and close operations, was combined with visual principle to construct visual saliency maps, which highlighted ship targets.

Region Characteristics are solid bases for distinguishing targets from background clutters too. A weighted local difference measurement [30] was proposed to enhance targets and suppress background clutters simultaneously, followed by thresholding to extract real targets. In [31], a Haar classifier was constructed by learning sea background features from feeding images, and this classifier was used to detect vessels. Geometrical analysis was also one way to distinguish target regions from different clutter regions [11]. Furthermore, the multi-direction gradient map was utilized to calculate the derivative entropy in [32], where the derivative entropy was adopted to measure targets’ local contrast for segmentation. The [33] filtered original images with high-boost filters at first to enhance target signals, then, the multiscale analysis was used to measure targets’ local contrast for the following adaptive threshold.

Sparse Representation is one efficient way to show the geometrical features of an infrared image. An over-complete dictionary based sparse representation with the Gaussian filtering was proposed to find the target’s model [34]. A patch-image model was proposed to take advantage of the non-local, self-correlation of the image background, which could formulate the target detection as optimizing the sparse matrices’ recovery [35]. Apart from these, the image decomposition based on Laplacian sparse representation [36] and sparse ring representation [37] was also proposed to work on robust infrared maritime target detection. In [38], the sparse representation was used to capture targets’ edges from a local saliency map. [39] described background and targets with a

background over-complete dictionary and a generalized Gaussian target over-complete dictionary, respectively. Then, the sparse representation energy which distinguish targets from background distinctly was exploited to extract targets.

The most fundamental method to extract targets is based on the **Pixel Characteristic Analysis**. Feature points defined by the local gradient and contrast were first extracted in [40] and used for motion prediction, then, background and foreground could be segmented via these characteristics. Each pixel's intensity contrast to its neighbor background was taken advantage of in order to measure the dissimilarity between each location and the neighborhoods, by which the target pixel can be enhanced to be easily distinguished from background pixels [41]. Each pixel's relative local contrast was also measured with multiscale analysis method in [42] to suppress background. A fast grayscale-thermal foreground detection was applied with collaborative low-rank decomposition method in [43, 44]. Thermal and RGB sensors were used for the tracking of the targets in [45]. Furthermore, a local steering kernel was proposed in [46] to help measure the local contrast of each pixel for target segmentation.

Unfortunately, even though lots of state-of-the-art DBT algorithms show up, it is still desperately needed for the efficient DBT algorithm that can work well specifically when there are strong ocean waves or both strong and weak small targets show up in the same scene. This kind of algorithms will make a great difference towards improving the success rate and efficiency of maritime missions in some severe weather conditions.

III. IMAGE ENHANCEMENT BASED ON THE LPSM

This section elaborates why and how to suppress wave clutters and enhance targets by the LPSM in three parts: Part A analyzes the characteristic difference between the target's peak and the waves' peaks in local areas. Part B explains the proper way to measure the local singularity of each peak and how to enhance the original infrared maritime image. Finally, Part C gives the complete algorithm flow of the LPSM-based image enhancement.

A. Local Peak Singularity of Waves and Targets

Three key points need to be clarified before analyzing the local singularity of each peak: *Peak Detection*, *Local Area Size*, and *Local Characteristic Indexes*. In this part, these three points will be introduced in sequence. Finally, detailed data will be given to support the conclusion that the target peak is locally singular and wave peaks are not.

1) Peak Detection

In this paper, a peak is defined as one image pixel with the locally outstanding intensity. It can be acquired by filtering each pixel with the Peak Kernel given in Eq. (1), where the M and N are the width and height of the kernel, respectively.

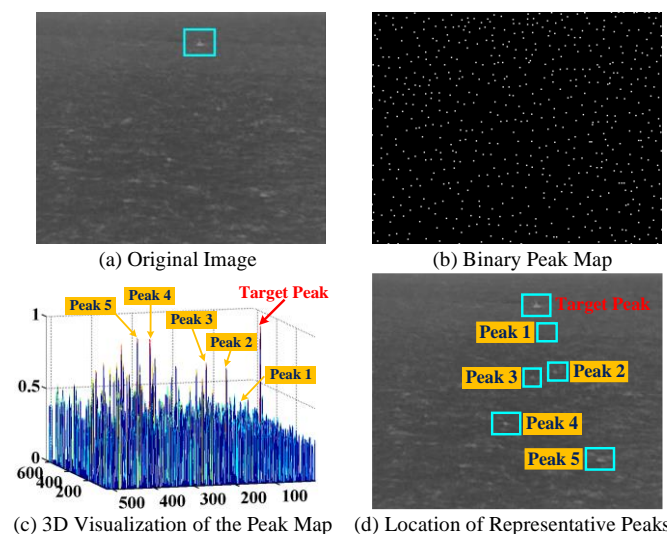
For each pixel, if its filtered value is positive, it would be classified as one peak. This peak definition tries to keep as many feature points as possible compared with traditional peak definitions, like the local maximum [41].

$$PKernel = \frac{1}{N \times M - 1} \begin{bmatrix} -1 & \dots & -1 \\ \vdots & N \times M - 1 & \vdots \\ -1 & \dots & -1 \end{bmatrix} \quad (1)$$

To preserve the most representative peaks, a peak screening mechanism is performed. This means if two peaks are too close to each other, the weaker pixel will be removed. In our case, $M=N=5$ is selected so that the local maximum peaks can be reserved and the weaker peaks can be removed if they are less than 5 pixels away from the stronger peak. If they have equal intensities, the leftmost one will be reserved.

Here, each target or wave clutter is represented by its own peaks. In this way, the original image can be reconstructed by generating a peak map, which is helpful for analyzing the local intensity characteristic of the target and wave clutters.

Fig. 1(a) is a typical infrared maritime image containing one fishing boat target marked with a rectangle. After the peak detection, its binary peak map is given in Fig. 1(b) where the peak pixel is marked in white and the non-peak pixel is marked in black. Fig. 1(b) shows the selected peaks in binary image and it can be seen that the peak pixels are not closer than 5 pixels to each other. The corresponding peak map is shown in a 3D view of Fig. 1(c) for convenience.



(c) 3D Visualization of the Peak Map (d) Location of Representative Peaks
Fig. 1 Demonstration for a typical peak map and its representative peaks.

From the 3D view of the Peak Map, it can be seen that the target peak stands out in its local area because all of its surrounding peaks have much weaker intensities than the target peak. On the contrary, wave clutter peaks are surrounded by peaks with similar intensities. This indicates that the target peak is locally singular, and wave clutter peaks are not.

2) Local Area Size

Before comparing the local singularity of different peaks, it is necessary to decide the neighborhood size in which the local peak singularity should be measured. Considering that ocean waves have a periodic motion pattern, its intensity distribution characteristic can be demonstrated in several wavelengths. So, it is reasonable to use one wavelength's corresponding length in the image as the neighborhood size unit.

In this paper, it is presumed that ocean waves obey the basic wave relationship of Eq. (2), where the λ is the wavelength, the

v and T are the wave speed and the period of ocean waves, respectively [47].

$$\lambda = v \times T \quad (2)$$

To calculate the wavelength λ , we need to introduce another relationship between the wavelength λ and the wave speed v in Eq. (3) [48] since the wave speed v is unknown.

$$v = \sqrt{\frac{g\lambda}{2\pi} \times \tanh\left(2\pi \frac{d}{\lambda}\right)} \quad (3)$$

In this above equation, the variable g is the gravitational acceleration and d is the ocean depth. In order to find the wave speed, the wind speed and the period of the waves are used. The wind speed is calculated in real time to obtain the wavelength. The gravitational acceleration and the ocean depth are used depending on the region.

Each ocean wave consists of complex frequency components. In order to acquire the wave period T , the frequency component which contributes the most to the wave energy would be used as the representative component to calculate the wave period. The P-M power spectrum [49] is a widely used method to analyze the connection between the ocean wave frequency components and their energy contribution. It can be expressed in Eq. (4). Eq. (4) includes a numerical constant α of 0.0081 and a numerical constant β of 0.74. $U_{19.4}$ represents the wind speed at 19.4m above the sea surface.

$$S_{PM}(\omega) = \frac{\alpha g^2}{\omega^5} \times \exp\left[-\beta \times \left(\frac{g}{\omega \times U_{19.4}}\right)^4\right] \quad (4)$$

According to this equation, the power spectrum of ocean waves in Fig. 1(a) is shown in Fig. 2. The wind speed is measured in real time, and the wind scale and mean wave height are looked up in the Beaufort Wind Scale Table according to the real-time measured wind speed.

As marked in Fig. 2, the strongest frequency component exists at 0.8859 rad/s. Referring to Eq. (5), the corresponding wave period is 7.0922s.

$$T = \frac{2\pi}{\omega} \quad (5)$$

Using this information, the wavelength can be calculated by combining the Eq. (2) and (3). It turns out that the wavelength is 78.4527m.

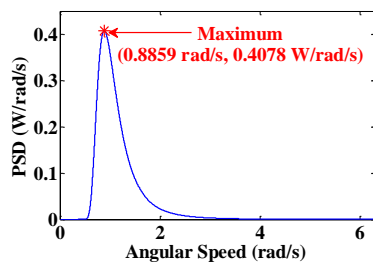


Fig. 2 The power spectrum of ocean waves in Fig. 1(a), where the wind speed at 19.4m above the sea surface is 9.7 m/s.

The spatial resolution of the mid-infrared thermal imager we have used to take the Fig. 1(a) is 3.75m, so the length of one wavelength in image is 20.92 pixels, approximated to 24 pixels. In this paper, ten wave wavelengths is set as the neighborhood size. That is to say that the area radius for measuring the local

peak singularity would be 210 pixels. The number of wavelengths is obtained based on the empirical experiments. It was found that if decreasing this radius, the clutter peak's local singularity would be increased. Thus, the target peak's advantage can be weakened. On the contrary, if increasing this radius, the target peak's local singularity can be attenuated, especially when strong clutter peaks exist.

3) Local Characteristic Indexes

In order to measure the local singularity of each peak compared with its neighbor peaks, we propose to use five different indexes to measure each peak's local characteristics. The first two indexes are **Peak Intensity (PI)** and **Number of Neighbor Peaks (NNP)**.

The third index is the **Average Exponent Difference (AED)**. For the peak a and b , their exponent difference can be calculated according to Eq. (6), where the s represents the exponent difference and it is in the range of $-1 \sim 1$. The peak a and b represent two neighbor peaks and we have named these two peaks with a and b to simplify the general peak characterization process. The greater the absolute value of s , the stronger the singularity. Besides, the sign function $\text{sgn}(\cdot)$ is used to give a positive value if a is greater than b , or a negative value if b is equal or greater than a . In this way, it would be easy to tell whether a peak is stronger or weaker than its neighbor peaks.

$$s = \text{sgn}(a-b) \times \left[1 - \exp\left(-sf \times \frac{|a-b|}{\min(a,b)}\right)\right] \quad (6)$$

The factor sf in Eq. (6) is the singularity factor, which is calculated according to Eq. (7).

$$sf = -\frac{\ln(\min(s))}{\text{maxdiff}} \quad (7)$$

In this equation, maxdiff is the difference between the greatest and smallest intensity values in an infrared maritime image. Besides, the $\min(s)$ is set to 1×10^{-8} to guarantee it is calculable on the computer. Then, the AED can be obtained by the Eq. (8), where N represents the number of neighbor peaks and s_{ci} is the exponent difference between the central peak and its i^{th} neighbor peak.

$$AED = \frac{\sum_{i=1}^N s_{ci}}{N} \quad (8)$$

The fourth index is the **Average Peak Difference (APD)** in Eq. (9) where P_c is the intensity of the central peak in a local area and P_i is the intensity of each neighbor peak.

$$APD = \frac{\sum_{i=1}^N (P_c - P_i)}{N} \quad (9)$$

The fifth index is the **Average Relative Peak Difference (ARPD)** defined as Eq. (10).

$$ARPD = \frac{\sum_{i=1}^N (P_c - P_i)}{N \times P_c} \quad (10)$$

The comparison among these five indexes is summarized in Table II.

TABLE II
LOCAL SINGULARITY INDEXES

Index	Reflected Peak Characteristic
PI	The original peak height
NNP	The density of local peaks
AED	The amplified average intensity difference between the central peak and its neighbor peaks that have large intensity gaps from the central peak
APD	The original average intensity difference between the central peak and all its neighbor peaks
ARPD	The relative APD to PI, or the absolute intensity advantage of the central peak

It can be seen that these five indexes show the local peak characteristics in terms of intensity (PI/AED/APD/ARPD) and density (NNP). Since these two factors could determine a peak's advantage for the saliency competition in a local area, these five indexes can be qualified for analyzing a peak's local saliency, namely, the local singularity (the more saliency, the more visually singular).

4) Local Characteristic Comparison between the Target Peak and Clutter Peaks

Based on the above introduction, the local singularity comparison among six representative peaks is given in Table III. Detailed data analyses will be shown in Sec. V-A.

In Table III, the Dominant Peak refers to the peak that has the greatest index value among six representative peaks. The Interferential Peak identifies the clutter peak that competes with the target peak for global saliency. Lastly, the Globally Dominant column tells whether the dominant peak is globally dominant compared with all clutter peaks.

Compared with the five clutter peaks, the target peak has the greatest local characteristic values in terms of PI, AED, APD and ARPD, but it is overwhelmed by Peak 1 in NNP. Peak 5 also stands out in PI, which means the target peak loses its absolute predominance in this characteristic index. When globally compared with all clutter peaks in the image, the target peak loses its advantage in PI and NNP.

TABLE III
THE COMPARISON AMONG FIVE LOCAL SINGULARITY INDEXES WITH THE NEIGHBOR AREA RADIUS OF 210 PIXELS

Index	Dominant Peak	Interferential Peak	Globally Dominant
PI	Target Peak, Peak 5	Peak 5	No
NNP	Peak 1	Peak 1	No
AED	Target Peak	None	Yes
APD	Target Peak	None	Yes
ARPD	Target Peak	None	Yes

Even though the target peak cannot always remain dominant to all clutter peaks in terms of the PI and NNP, it can stand out in the AED, APD and ARPD. Table III shows that the target has the absolute advantage in these three indexes compared with global clutter peaks. This means that the target peak is locally singular and clutter peaks are not in terms of the AED, APD and ARPD. So, one way to suppress wave clutters and enhance targets could be weakening each pixel intensity that has low local peak singularity and enhancing the one with high local peak singularity.

B. Implementation Method for Image Enhancement

Part A has proved that the local peak singularity could be a robust reference to distinguish the target peak from wave clutter peaks, which is significant for the wave suppression and the target enhancement. This part will explain how to measure the local peak singularity in a proper way that can regulate the LPSM to further widen the local singularity gap between the target peak and wave clutter peaks. The original infrared maritime image could then be enhanced according to this regulated LPSM.

Part A shows that the locally singular peak has a greater average peak height difference than others. In other words, the more similar neighbor peaks, the weaker local peak singularity. To amplify this characteristic, only neighbor peaks whose intensities fall into the range of 0.8~1.2 of the central peak's intensity will contribute to the local singularity of the central peak. And the more contributing neighbor peaks, the less local peak singularity.

The local singularity is an attribute that focuses on the object's feature expression in a local area. With the increase of the local area size, this attribute could be weakened. In other words, the nearer the contributing neighbor peaks, the more it contributes to the central peak's local singularity. So, it is reasonable to stipulate that each difference between the contributing neighbor peak and the central peak should be weighted by their distance, and this weight factor is shown in Eq. (11).

$$w_i = 1 - \frac{d_i}{R} \quad (11)$$

In Eq. (11), R is the radius of the circular local area centered on the central peak. It is equal to ten wavelengths of the ocean waves. The factor d_i represents the Euclidean distance between the neighbor and the central peaks. It is calculated by Eq. (12).

$$d_i = \sqrt{(x_i - x_c)^2 + (y_i - y_c)^2} \quad (12)$$

The coordinates (x_i, y_i) locates the i^{th} contributing neighbor peak. And (x_c, y_c) represents the position of the central peak.

Referring to the data in Part (A-4), the locally singular peak, like the target peak, typically has stronger local characteristic values than its neighbor peaks. So, compared with the central peak, the weaker contributing neighbor peaks should increase the central peak's local singularity, while the stronger ones should decrease the central peak's local singularity. Besides, the bigger the difference, the more the neighbor peak could make a difference to the central peak's local singularity.

Based on this analysis, the local singularity of the central peak could be measured according to Eq. (13).

$$S_c = \frac{\sum_{i=1}^N w_i \times (P_c - P_i)}{N \times P_c} \quad (13)$$

In Eq. (13), the quantified local singularity of the central peak is given by S_c . N is the number of contributing neighbor peaks. P_c and P_i represent the intensities of the central peak and the i^{th} neighbor peak, respectively. The normalized weight

factor \bar{w}_i is calculated in Eq. (14). The reason for adopting a normalized weight factor \bar{w}_i is to make sure that the quantified local singularity S_c will not exceed 1.

$$\bar{w}_i = \frac{w_i}{\sum_{j=1}^N w_j} \quad (14)$$

In order to suppress the wave clutter peaks and enhance the target peak, the original intensity needs readjusting based on their local peak singularity values. However, it is inevitable to have a target whose intensity is lower than wave clutters, so we propose to readjust the intensity of each peak by Eq. (15) where $\max(P)$ is the highest intensity of the original image.

$$P'_c = P_c + [2 \times \max(P) - P_c] \times S_c \quad (15)$$

The readjusted peak intensity P'_c is drawn to the preset up limit $2 \times \max(P)$ if it has a positive local peak singularity S_c . The greater the value of S_c , the closer P'_c is to the upper limit. Considering that the clutter peak's singularity is much lower than the target peak's, this intensity readjustment equation guarantees that the readjusted target peak could have a higher intensity than clutter peaks even if its original intensity is much lower. In other words, the readjusted intensity has a positive correlation to the peak's local peak singularity.

After readjusting each peak's intensity, a sampled enhancement map can be generated by dividing each readjusted peak intensity by the corresponding original peak intensity.

Then, the complete enhancement map can be generated by interpolating the sampled enhancement map. In our model, we adopt the Cubic Convolution Interpolation [50] to construct this enhancement map. Its convolution kernel in one dimension is given in Eq. (16).

$$w(x) = \begin{cases} 1.5|x|^3 - 2.5|x|^2 + 1 & \text{for } |x| \leq 1 \\ -0.5|x|^3 + 2.5|x|^2 - 4|x| + 2 & \text{for } 1 < |x| \leq 2 \\ 0 & \text{otherwise} \end{cases} \quad (16)$$

Finally, the enhanced image can be acquired by Eq. (17).

$$EI = \text{norm}(OI \bullet EM) \quad (17)$$

In Eq. (17), EI is the enhanced infrared maritime image, OI represents the original image and EM is the complete enhancement map. The operator \bullet means the dot product of two vectors and $\text{norm}(\cdot)$ normalizes the image.

The complete algorithm flow of the LPSM-based image enhancement will be shown in Fig. 3, where the key intermediate results based on the normalized original image are given in 3D views.

It can be seen from the peak map that the original target peak does not have the advantage over clutter peaks in terms of the intensity. However, after readjusting each peak's height according to their local singularity, the target peak stands out obviously thanks to its overwhelming local singularity in the local peak singularity map.

An EM is generated after surface fitting based on the sampled enhancement map. This EM has a flat surface fluctuating around 1.0000 where wave clutters exist and a protuberant peak reaching up to 1.8470 where the target is located. After multiplying the original infrared maritime image (IMI) by this EM, the target's intensity gets about 1.8470 times stronger while guaranteeing wave clutters' intensities will not be improved. If normalizing this enhanced image into the range of 0~1, the wave suppression and target enhancement can be achieved since the target area becomes the brightest area and wave clutters get weakened.

IV. TARGET SEGMENTATION BASED ON THE GDSCSB

The LPSM-based image enhancement helps improve the image quality for observing and detecting targets. This section works on segmenting real targets from the enhanced IMI based on the GDSCSB.

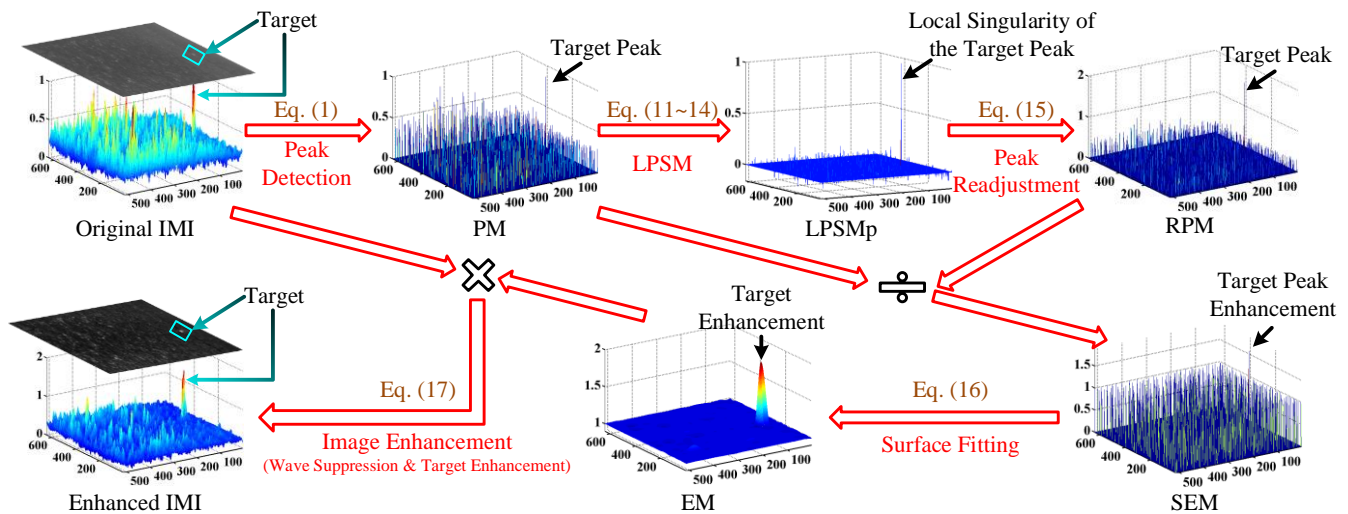


Fig. 3 The visual expression for the algorithm flow of the LPSM-based image enhancement. In this illustration, all abbreviations in this figure and the following Pseudo-Code I mean: IMI (Infrared Maritime Image), PM (Peak Map), LPSMp (Local Peak Singularity Map), RPM (Readjusted Peak Map), SEM (Sampled Enhancement Map), EM (Enhancement Map).

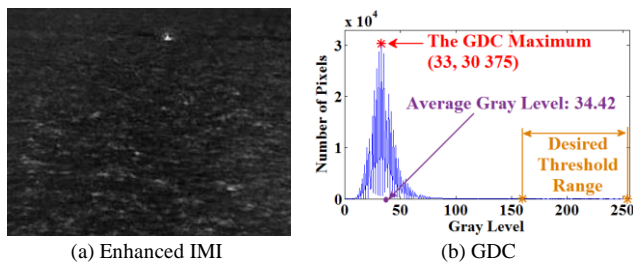


Fig. 4 The enhanced IMI in Fig. 3 and its GDC. The GDC is generated by connecting the top points on bars of the histogram.

TABLE IV
DETAILED INFORMATION OF THE DTR

DTR	Pixel Number's Ratio in All	Number of All Pixels
160~254	0.253%	327 680

The image binarization is an efficient way to extract the image area of interest when the desired threshold is available. Take the enhanced IMI in Fig. 4 for example. Because the target is small and does not show up in many places, traditional local binarization methods cannot be used since they apply different thresholds for different image cells [51]. Otherwise, a lot of wave clutters would be included. So a global threshold is desired.

To extract the real target and remove all wave clutters, it was found that the threshold should be in a certain range which is labeled as the desired threshold range (DTR) in Fig. 4(b). Detailed information of this DTR is given in Table IV.

For calculating the desired threshold, we found from Fig. 4(b) and Table IV that one feature could be exploited: the strong single-peak feature. That is to say the DTR covers only 0.2533% of all 327,680 pixels and the rest 999.7467% pixels gather around the global maximum point.

Due to this feature, the global average gray level (defined as Eq. (18) where the $GDC(i)$ represents the value of i^{th} point on the GDC. N is the number of gray levels) is only 1.42 horizontally away from the global peak at (33, 30375).

$$AGL = \frac{\sum_{i=1}^N i \times GDC(i)}{\sum_{i=1}^N GDC(i)} \quad (18)$$

If the GDC is shifted rightwards to move the global peak into the DTR, the average gray level of the shifted GDC (SGDC) could be a desired threshold. Besides, to avoid increasing the calculated threshold unexpectedly, the rightward cyclic shift is adopted here to guarantee that no points on GDC would be moved beyond the original maximum gray level.

It was found out that the desired shift distance is the horizontal distance from the global maximum point to the midpoint between the maximum of gray level range and the first zero-point right to the global maximum point on GDC. This is illustrated in Fig. 5.

However, the image contrast is improved to a great extent after enhancement. This leads to a discrete gray level distribution. Thus, the first right zero-point could be leftwards deviated from its supposed position, which results in decreasing the desired shift distance. To solve this problem, we propose to

find the desired zero-point based on the fitted envelope:

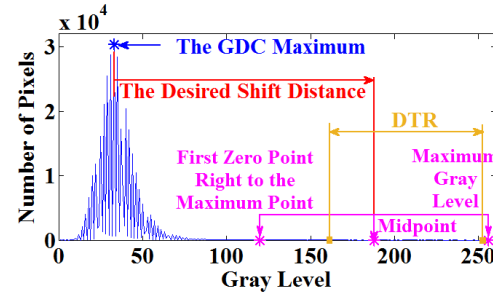


Fig. 5 Illustration of the desired shift distance

1) All local maximums on the GDC are sampled according to Eq. (19).

$$GDC(i) \geq GDC(i-1) \ \& \ GDC(i) \geq GDC(i+1) \quad (19)$$

2) According to the sampled local maximum points, the least square method is used to generate a high degree polynomial like Eq. (20). In our method, the degree n is set to 20 to help find the desired zero-point.

$$f(x) = a_n x^n + a_{n-1} x^{n-1} + \dots + a_2 x^2 + a_1 x \quad (20)$$

3) Find the first zero-point right to the global maximum on the fitted curve. Since this envelope fitting abandons all discrete zero-points on the original GDC, it can be regarded as a low-pass filtering process. Thus, the ‘‘Ring Effect’’ of the low-pass filtering determines that the desired zero-point could always occur on the transition from the sharp incline to its right flat curve.

After confirming the desired zero-point, the midpoint between it and the maximum of the gray level range can be found. Thus, the shift distance can be obtained by Eq. (21)

$$SD = X_{MP} - X_{Mx} \quad (21)$$

In the above equation, X_{MP} and X_{Mx} are the abscissas of the midpoint and the GDC maximum point, respectively.

With the shift distance, the rightward cyclic shift can be performed on the original GDC according to Eq. (22).

$$X_{SGDC}(i) = [X_{GDC}(i) + SD] \% (X_{MGL} + 1) \quad (22)$$

In Eq. (22), the $X_{SGDC}(i)$ and $X_{GDC}(i)$ represent the abscissas of the i^{th} point on the SGDC and original GDC, respectively. X_{MGL} is the abscissa of the image maximum gray level. The operator $\%$ keeps the remainder after the division.

Finally, the desired threshold can be obtained by rounding off the average gray level of the SGDC. Using the enhanced IMI in Fig. 4, related data of this operation are given in Table V, where all abbreviations are defined as Eq. (21) and (22).

Table V shows that after shifting the original GDC, the obtained threshold 173 is the desired one for detecting targets from the enhanced IMI. The whole operation flow of this GDC cyclic shift is shown in the Fig. 6.

TABLE V
RELATED DATA OF THE DESIRED THRESHOLD CALCULATION

X_{Mx}	X_{MP}	SD	Shifted X_{Mx}	DTR	Obtained Threshold
33	170	137	170	160~255	173

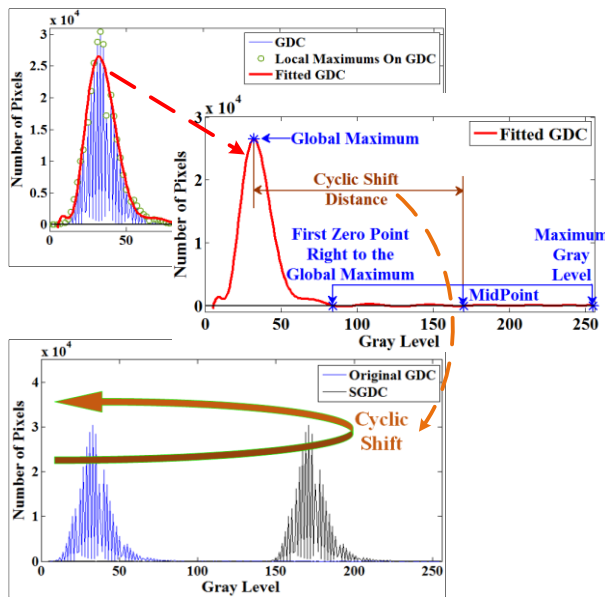


Fig. 6 Algorithm flow of the desired threshold calculation based on the rightward cyclic shift of the GDC.

V. EXPERIMENTS AND ANALYSES

In this section, Part A introduces our datasets for algorithm verification. Part B gives the detailed local peak singularity index data based on each representative IMI to further support the conclusion in Sec. III-A. In parts C & D, experiments and evaluations for the LPSM-based image enhancement and GDCSB-based target segmentation will be made in order. Part E will compare five existing algorithms with the proposed.

A. Datasets Introduction

Our datasets for algorithm verification consist of 16 different IMI sequences, including 13,625 IMIs in total. These IMI sequences are taken under different environmental conditions and contain various targets. 12 IMI sequences were captured using a mid-wave infrared (MWIR) refrigeration thermal imager. This MWIR imager has an effective response band of 3.7~4.8 μm and a resolution of 640 \times 512. Four other IMI

sequences were captured by a long-wave infrared (LWIR) thermal imager. The effective response band of the LWIR is 8~12 μm and its resolution is also 640 \times 512.

Detailed information about these 16 IMI sequences are given in Table VI. In this table, the 16 IMI sequences are divided into two categories by obviously visible background clutters (OVBC) and invisible background clutters (IVBC).

In our datasets, sequences (A~J) belong to OVBC. The sequences (A, C, D, & E) have background clutters caused by ocean waves and sun-glints. Sequences (B, F, H, & I) contain both wave and cloud clutters. Background clutters in sequences (G & J) are caused by ocean waves and moon-glints. The other six sequences (K~P) fall into IVBC. IMIs in these sequences have smooth backgrounds.

These 16 IMI sequences have various infrared maritime targets with different intensities and local contrasts. Targets in sequences (A~D, G, H, J, & O) are all fishing boats. Sequences (E, C, M, & P) have yachts on sea surface. A ro-ro ship exists in the sequence F. Sequences (L, N, & P) contain swimmers. These various infrared maritime targets are also shown in different intensities and local contrasts which will be demonstrated in the following Part C.

Since these ten IMI sequences were captured in two different wave bands, the proposed algorithm's performance in different infrared wave bands can be well verified, too.

All in all, these datasets can soundly verify the proposed algorithm's performance with different backgrounds, various targets, and changing infrared wave bands.

B. Local Singularity Index Data

The high local singularity of target peaks is the basis of LPSM-based image enhancement. To show this feature more comprehensively, this part will give the local singularity index data of each target in representative IMIs and compare them with background clutters. When calculating the local singularity index data on each representative IMI, the local area radii defined as in Sec. (III-A-2) are listed in Table VII.

TABLE VI
DETAILED INFORMATION OF EACH IMI SEQUENCE

Category	IMI Sequence	Sequence Length	Wave Band	Number of Targets	Target Types	Wind Speed (m/s)	Wind Scale	Mean Wave Height (m)	Temperature (°C)	Capture Time
OVBC	A	250	MWIR	1	Fishing Boat	9.7	5	2.0	8	15:41
	B	950	MWIR	2	Fishing Boat	8.6	5	2.0	6	15:16
	C	250	MWIR	4	Fishing Boat	8.6	5	2.0	6	15:30
	D	1250	MWIR	2	Fishing Boat	9.7	5	2.0	8	10:00
	E	450	MWIR	1	Yacht	9.2	5	2.0	8	11:08
	F	975	MWIR	1	Ro-ro Ship	9.5	5	2.0	7	10:50
	G	1450	MWIR	2	Fishing Boat	3.5	3	0.6	2	17:20
	H	1250	LWIR	2	Fishing Boat	9.7	5	2.0	8	10:00
	I	375	LWIR	1	Raft	3.8	3	0.6	10	14:20
	J	1400	LWIR	1	Fishing Boat	4.0	3	0.6	2	19:20
IVBC	K	1900	MWIR	1	Yacht	6.7	4	1.0	10	13:00
	L	250	MWIR	1	Swimmer	2.5	2	0.2	11	9:30
	M	500	MWIR	1	Yacht	6.2	4	1.0	10	13:50
	N	1500	MWIR	1	Swimmer	1.0	1	0.1	19	13:31
	O	375	MWIR	2	Fishing Boat	5.8	4	1.0	10	14:05
	P	500	LWIR	3	Yacht & Swimmer	2.9	2	0.2	11	10:00

The wind speed and air temperature are measured in real time, and the wind scale and mean wave height are looked up in the Beaufort Wind Scale Table according

to the real-time measured wind speed.

TABLE VII
THE LOCAL AREA RADII WHEN CALCULATING LOCAL SINGULARITY INDEX
DATA ON EACH REPRESENTATIVE IMI

IMI	A	B	C	D	E	F	G	H
Radius (px)	210	247	100	150	188	201	163	205
IMI	I	J	K	L	M	N	O	P
Radius (px)	200	160	249	104	70	90	163	150

In order to measure how much the target peak stands out from clutter peaks in terms of a specific local singularity index, two different separation degree indexes are proposed here. One is the absolute separation degree (ASD) defined as Eq. (23), where C_{TP} is the local characteristic value of the target peak and C_{GB} is the greatest local characteristic value of clutters.

$$ASD = \frac{C_{TP} - C_{SB}}{C_{SB}} \quad (23)$$

The ASD determines the separation degree of the target to all strong background clutters on the premise of zero false alarms. A positive ASD means the target peak can be completely separated from all clutter peaks in the corresponding local singularity index. The higher the ASD, the easier it is to detect the target with no false alarms, namely, a zero FAR.

The other separation degree index is the relative separation degree (RSD) defined as Eq. (24) where C_{AVG} gives the average

characteristic value of background clutter peaks.

$$RSD = \frac{C_{TP} - C_{AVG}}{|C_{AVG}|} \quad (24)$$

The RSD shows the relative separation degree of the target to the image background. A positive RSD means the target peak's local singularity is stronger than the average of all background clutters. The higher the RSD, the lower the MAR.

Using 16 representative IMIs shown in the following Part C, we calculated each target peak's ASD and RSD in terms of PI, NNP, AED, APD and ARPD. To show this data in a more visual way, it is displayed in the graphs of Fig. 7.

In terms of PI, all targets have positive RSDs, which means target peaks' PIs are over the average of all background clutter peaks' PIs. However, the ASD data demonstrates that targets failed to stand out when compared with strong background clutters. 5 targets (T1, T3, T7, T14, & T15) have non-positive ASDs. This means some strong background clutter peaks have the same or even greater PI values with these targets. Thus, PI fails to help targets beat the strong background clutters.

For NNP, all targets have negative ASDs and 14 targets have negative RSDs. Thus, compared with background clutters, targets do not have dominant local singularity in terms of NNP.

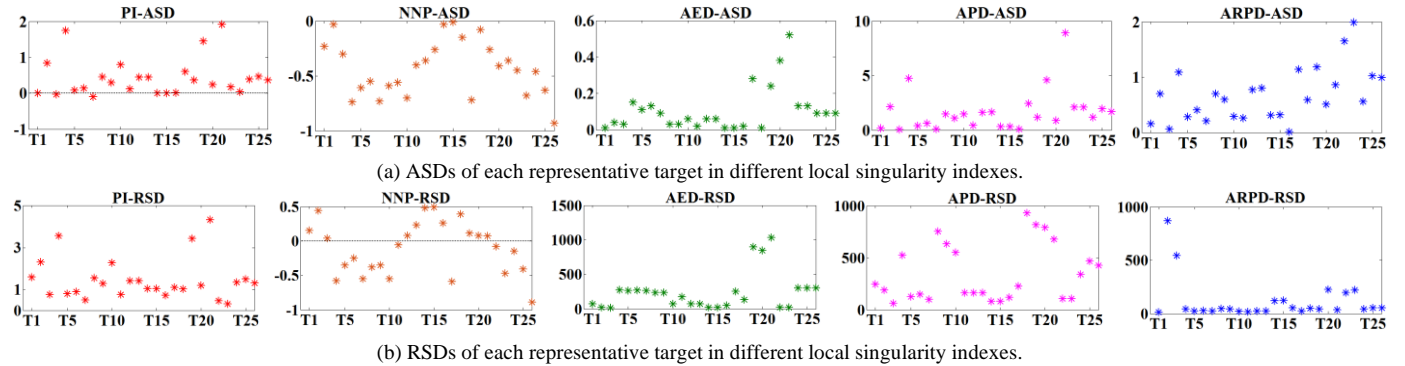


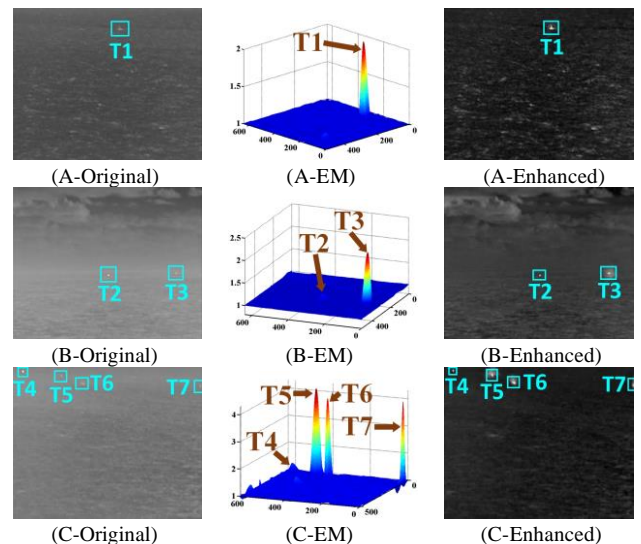
Fig. 7 Separation degrees of each representative target in terms of different local singularity index. In 16 representative IMIs, there are 26 targets in total. Thus, in each graph, the abscissa axis lists all targets numbered from T1 to T26, and the ordinate axis gives separation degree values.

When it comes to AED, APD, and ARPD, all targets acquire positive ASDs and RSDs. This demonstrates that, compared with all background clutters, every target has dominant local characteristic in terms of AED, APD, and ARPD. In conclusion, these three indexes give all targets higher local singularity than all background clutters.

The above analyses further support the conclusion in Sec. III-A that the target peak is locally singular and clutter peaks are not in terms of the AED, APD, and ARPD.

C. Evaluation of the LPSM-Based Image Enhancement

Fig. 8 shows the performance of the LPSM-based image enhancement on each representative IMI. The first column lists original representative IMIs. The second column shows each enhancement map (EM). The enhanced IMIs are posted on the third column.



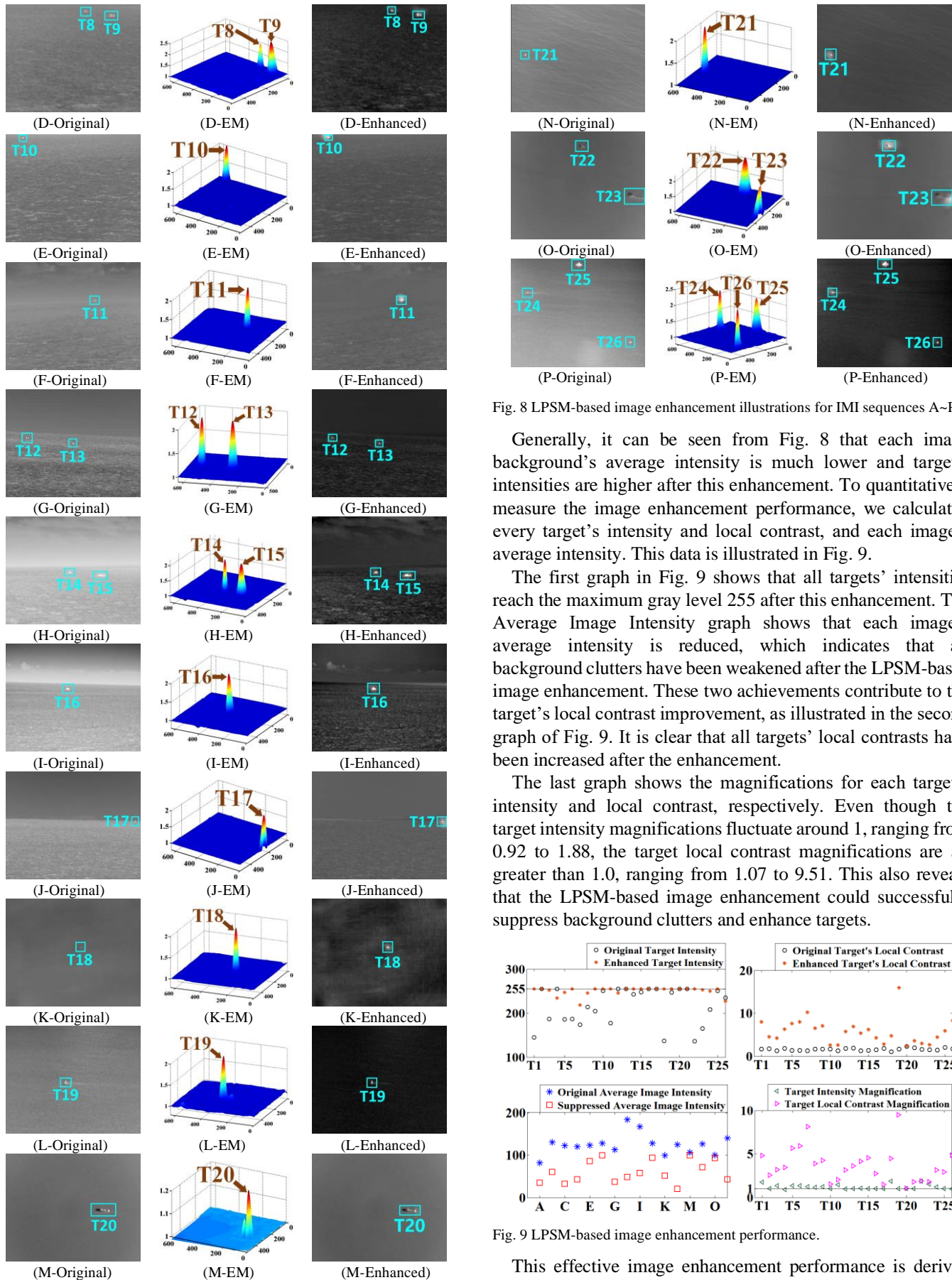


Fig. 8 LPSM-based image enhancement illustrations for IMI sequences A-P.

Generally, it can be seen from Fig. 8 that each image background’s average intensity is much lower and targets’ intensities are higher after this enhancement. To quantitatively measure the image enhancement performance, we calculated every target’s intensity and local contrast, and each image’s average intensity. This data is illustrated in Fig. 9.

The first graph in Fig. 9 shows that all targets’ intensities reach the maximum gray level 255 after this enhancement. The Average Image Intensity graph shows that each image’s average intensity is reduced, which indicates that all background clutters have been weakened after the LPSM-based image enhancement. These two achievements contribute to the target’s local contrast improvement, as illustrated in the second graph of Fig. 9. It is clear that all targets’ local contrasts have been increased after the enhancement.

The last graph shows the magnifications for each target’s intensity and local contrast, respectively. Even though the target intensity magnifications fluctuate around 1, ranging from 0.92 to 1.88, the target local contrast magnifications are all greater than 1.0, ranging from 1.07 to 9.51. This also reveals that the LPSM-based image enhancement could successfully suppress background clutters and enhance targets.

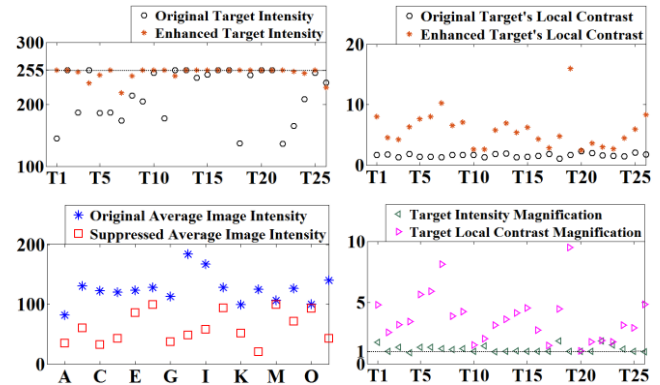


Fig. 9 LPSM-based image enhancement performance.

This effective image enhancement performance is derived from the EMs as shown in the second column of Fig. 8. It can be

seen that all EMs have flat foundations and towering peaks where targets locate. Thus, after multiplying the original IMI by the EM, targets' local contrasts can be amplified. In Fig. 8, M-Enhanced increases the difference between the gray seawater background and bright target region for an easier detection. The increased pixel value is not very visible in the images but the background in the M-Enhanced is darker than the original image. O-Enhanced increases the brightness of the background next to the ship but the peak value of the bright region is in the target area.

It can also be seen from (B-EM) and (C-EM) in Fig. 8 that when targets with various local contrasts appear in one IMI, the weaker target can get a higher peak in the EM and the stronger one will get a lower peak. This feature could narrow down the difference among targets' local contrasts in the enhanced IMI, which can make it easier to detect all targets simultaneously.

This can also be supported by the data in the last graph of Fig. 9. It is obvious that all weaker targets T3 and T5~T7 have greater magnifications than stronger targets T2 and T4.

In conclusion, after the LPSM-based image enhancement, targets are enhanced and image backgrounds are suppressed to a great extent. In addition, this method could narrow down the intensity/local contrast difference between stronger and weaker targets in the same image, guaranteeing a higher detection success rate.

D. Evaluation of the GDCSB-Based Target Segmentation

The key of the GDCSB-based target segmentation is to obtain the desired threshold for extracting targets from the enhanced IMI. The threshold calculation is based on the cyclic shift of the GDC which is generated from the enhanced IMI. Fig. 10 shows this GDC cyclic shift for each enhanced representative IMI in Fig. 8.

It is obvious that after the cyclic shift the original GDC's peaks have been moved to the corresponding DTRs successfully. This indicates that the average gray level of the SGDC will fall into the DTR, too.

For each graph in Fig. 10, the pentagram is in the corresponding DTR, which is marked by two asterisks. This indicates that the calculated thresholds for each enhanced IMI is in the DTRs. This can validate the proposed method for

desired threshold calculation. With the calculated desired thresholds, targets can be detected successfully.

E. Comparison with Existing Algorithms

This part compares the proposed algorithm with five existing algorithms based on our datasets. These algorithms are based on visual attention (VA) [18], wavelet transformation (WT) [2] and pixel local contrast (PLC) [41], human visual system (HVS) [16], and weighted local difference measure [30], respectively.

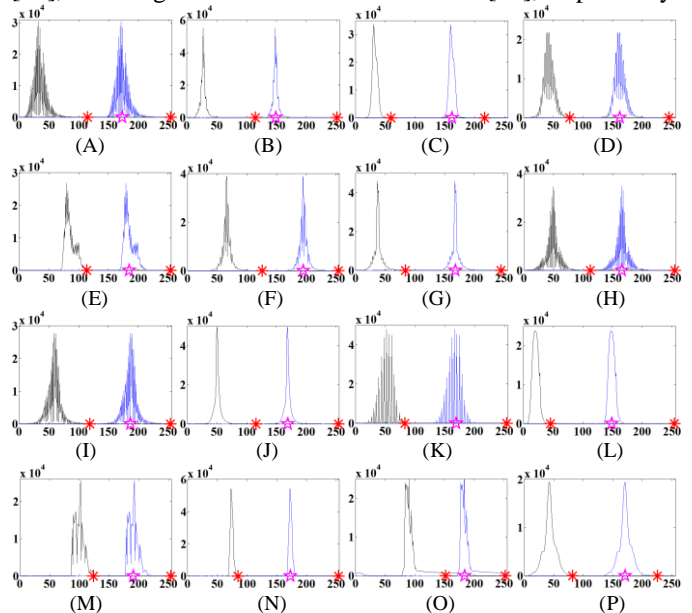


Fig. 10 The GDC cyclic shift for each enhanced representative IMI in Fig. 8. The abscissa axis of each graph represents the "Gray Level" and the ordinate axis is "Number of Pixels". The DTR for each enhanced IMI is marked by two red asterisks (**) and the calculated threshold is marked in a magenta pentagram (☆). The original GDCs are drawn in black curves and SGDCs are in blue curves.

Fig. 11 shows binary detection results of different algorithms using three typical IMIs in Fig. 8. In each binary image, all pixels that are judged as target pixels by the corresponding algorithm are shown as white. For visual convenience, we highlight true targets with green-yellow boxes and clutters are marked with orange boxes.

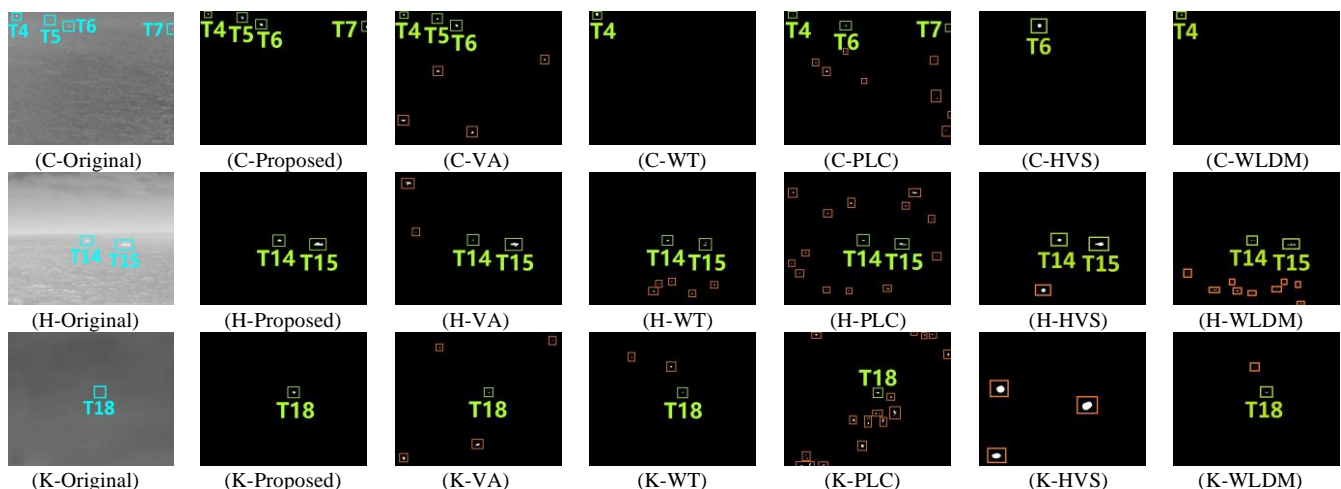


Fig. 11 Typical binary detection results of different algorithms. Detected targets are marked with green-yellow boxes and residual clutters are with orange ones.

TABLE VIII
DETECTION PERFORMANCE DATA OF DIFFERENT ALGORITHMS

IMI Sequence		A	B	C	D	E	F	G	H	I	J	K	L	M	N	O	P	Average	
MAR (%)	Proposed	0	0	0	0	0	0	0	0	0	0	0	0	0	0	0	0	0	0
	VA [18]	0	0	32.5	0	17.0	0	0	0	0	0	1.2	0	0	0	0	0	0	3.2
	WT [2]	0	0	69.0	0	0	5.0	0	0	0	0	15.0	0	0	0	0	0	0	5.6
	PLC [41]	0	0	28.8	0	0	0	0	0	0	0	0	0	0	0	0	0	0	1.8
	HVS [16]	0	50.0	75.0	41.5	77.1	0	31.2	0	0	0	100	0	0	0	0	0	57.9	27.0
	WLDM [30]	0	21.5	69.0	0	0	0	0	0	0	0	0	0	0	0	0	15.5	14.3	7.5
FAR (%)	Proposed	0.6	0	0	0	0.2	0	0.7	1.1	0	0	0	0	1.0	0	0	0	0	0.2
	VA [18]	73.1	51.3	59.1	33.6	85.3	80.8	46.9	50.5	82.1	62.9	77.1	13.0	54.6	1.0	1.5	0.37	48.3	
	WT [2]	75.1	7.0	13.3	67.3	56.5	92.2	72.3	71.6	78.9	76.2	69.6	14.5	52.4	47.4	33.3	0.33	51.7	
	PLC [41]	89.0	85.0	70.4	88.5	88.8	95.6	77.5	82.3	88.3	93.8	82.3	89.5	94.7	77.8	82.3	34.35	82.5	
	HVS [16]	35.1	37.9	0	8.6	57.4	30.6	1.4	38.1	19.4	46.2	100	0	0	0	0	0	23.4	
	WLDM [30]	94.4	1.9	3.9	89.6	93.1	96.5	2.4	84.7	33.3	42.2	6.5	1.0	0	0	37.9	0	36.7	

The worst detection results of five comparison algorithms occurred with the IMI (C). These five algorithms cannot detect all weak targets in this IMI. The WT, HVS, and WLDM even lost three weak targets. VA and PLC remained some wave clutters while missing T7 and T5, respectively. On the contrary, the proposed algorithm detected both strong and weak targets successfully and, meanwhile, removed all background clutters and background noise. The background noise from the brightness of the seawater depends on the temperature of the seawater in the thermal images. In case of bright seawater, the ship temperature would be brighter since the ship can get warmer than seawater. The formula for the wavelength was used to analyze the wave and ship difference in the images. In order to detect maritime targets for autonomous navigation, it is required to make decision a head of time. In our work, the far targets were detected to plan the navigation commands in advance. Ships with larger sizes would be easier to detect since the challenging task is distinguishing the small targets in clutter waves.

In terms of IMI (H) which is categorized as OVBC in Table VI, all six algorithms successfully detected targets. But five comparison algorithms failed to suppress all background clutters completely. This was true especially for PLC and WLDM, since they were sensitive to image local peaks, many clutters remained in the results. The VA cannot remove the interference from sea-sky line and clouds in IMI (H) because its visual attention mechanism was very sensitive to the object with high local contrast. The WT and HVS also kept some wave clutters. By contrast, our proposed algorithm removed all background clutters.

In terms of IMIs (K) categorized as IVBC in Table VI, all targets were detected by each algorithm except for the HVS. But VA, WT, PLC, and WLDM kept some wave clutters in the final detection results. For the algorithm HVS, it not only lost the true target but also remained three clutter areas. In conclusion, only the proposed algorithm had satisfactory performance on detecting targets; namely, detecting all targets and removing all background clutters.

To quantitatively compare the detection performance of these algorithms, MAR and FAR of different algorithms are calculated based on a total 13,625 IMIs. The MAR and FAR in this paper are defined as Eq.(25) and (26). In these two equations, MT is the number of missed targets, DT is the

number of detected targets, and FD is the number of false detection results in the form of residual background clutter. Detailed performance data is given in the following Table VIII.

$$MAR = \frac{MT}{MT + DT} \times 100\% \quad (25)$$

$$FAR = \frac{FD}{DT + FD} \times 100\% \quad (26)$$

Table VIII shows that all five comparison algorithms failed to detect all targets in IMI sequence C and their MARs were over 28.8%. When weak targets are accompanied with strong ones like in IMI sequence C, all five comparison algorithms only work on strong targets, overlooking weak targets' information. By contrast, the proposed algorithm could narrow the local contrast gaps between weak and strong targets by enhancing maps generated from local peak singularity measurement. Thus, the proposed algorithm lowered the MAR down to 0.

In addition, VA failed on IMI sequences E and K. WT could not detect all targets in IMI sequence K, either. WLDM lost many targets in sequences B, O, and P. The HVS generated the worst detection results since it failed on sequences B, D, E, G, K, and P (the most failed sequences of five comparison algorithms). This was because they had poor performance with extracting valid feature information from weak targets.

In terms of the average FAR, the proposed algorithm achieves 0.2%, 48.1% lower than VA, 51.5% lower than WT, 82.3% lower than PLC, 23.2% lower than HVS, and 36.5% lower than WLDM. Our proposed LPSM-based image enhancement and GDSCB-based target segmentation could suppress background clutters' features to a great extent, and then remove them from the final detection results completely. However, the five comparison algorithms could not suppress background clutters very well. That is why their detection results were interfered by these clutters intensively.

TABLE IX
THE COMPARISON OF PROPOSED AND DEEP LEARNING-BASED METHODS [52]

Method	Proposed	MRA	SVDNet	gcForest	RDF
Accuracy (%)	99.8	90.09	97.75	97.38	98.69
Time (s)	0.85	3.6	2.3	1.7	1.8

Our proposed algorithm outperforms the deep learning-based methods both in terms of computational time and accuracy. It is shown in Table IX that the proposed

algorithm provides 9.71% better detection than MRA, 2.05% better than SVDNet, 2.42% better than gcForest, and 1.11% better than RDF method. Computational time of the proposed algorithm is 2.75s, 1.45s, 0.85, and 0.95s lower than the deep learning-based methods, respectively.

These experiment results indicate that the proposed algorithm had much better performance on detecting infrared maritime targets in strong and weak background clutters, different wave bands, etc. When both strong and weak targets come up simultaneously, the proposed algorithm could detect them all successfully without losing weaker targets.

We also measured the average elapsed time of each algorithm on processing a single IMI. The detailed data are shown in Table X. These data were measured using MATLAB (X64) 2014b on Windows 10 Ultimate, running with an Intel Core i7-6700 processor and 16 GB of RAM.

TABLE X

THE AVERAGE ELAPSED TIME OF EACH ALGORITHM ON PROCESSING ONE IMI						
Method	Proposed	VA	WT	PLC	HVS	WLDM
Time (s)	0.85	0.36	0.23	10.83	0.26	5.7

Table X indicates that the PLC spent the most time on processing one IMI. This was because the PLC relied on too many loop operations on processing each image pixel. The same situation applied to the WLDM. Thus, these two algorithms spent much more time than other algorithms.

Our proposed algorithm spent 0.49s, 0.62, and 0.59s more than VA, WT, and HVS, respectively. This was mainly caused by the LPSM-based image enhancement where the PKernel (Eq. (1)) was used to filter each pixel.

Though our proposed algorithm was not the most efficient algorithm, but it outperformed all five comparison algorithms in detection accuracy. This would be very valuable for improving maritime target searching efficiency.

VI. CONCLUSION

This paper proposes a robust algorithm for infrared maritime target detection, which consists of the LPSM-based image enhancement and the GDCSB-based image binarization. Experiment results have shown that this algorithm has solid performance for different kinds of maritime targets in various situations, like strong ocean waves, multi-bands infrared imaging, etc.

The LPSM-based image enhancement can suppress background clutters and enhance real targets. In addition, the experiment results have shown that it can narrow down the local contrast gap between strong and weak targets. This helps increase the success rate of detecting both strong and weak targets simultaneously. The GDC cyclic shift makes sure that the gray levels covered by target pixels will be covered by background pixels which occupy the majority of all pixels. In this way, the average gray level of the SGDC could show the common intensity of all target pixels. This is how the GDCSB-based image binarization calculates the desired threshold for segmenting targets.

Our datasets include IMIs captured under different environments and in two infrared wave bands and have various maritime targets. Based on the comprehensive datasets, the

comparison among different algorithms demonstrate that the proposed algorithm has much better performance on infrared maritime target detection by lowering the MAR and FAR down to 0% and 0.2%, respectively. Thus, the accuracy of traditional infrared maritime searching system can be robustly improved.

ACKNOWLEDGMENT

We appreciate Fullah Fanary, Lauren Linkous and Andy Huynh for the paper proofreading.

TABLE XI
ABBREVIATIONS

LPSM	Local Peak Singularity Measurement
GDC	Grayscale Distribution Curve
GDCSB	Grayscale Distribution Curve Shift Binarization
SGDC	Shifted Grayscale Distribution Curve
EM	Enhancement Map
DBT	Detect-before-Track
FAR	False Alarm Rate
MAR	Missing Alarm Rate
LPSM	Local Peak Singularity Measurement
GDCSB	Grayscale Distribution Curve Shift Binarization
PI	Peak Intensity
NNP	Number of Neighbor Peaks
AED	Average Exponent Difference
APD	Average Peak Difference
ARPD	Average Relative Peak Difference
IMI	Infrared Maritime Image
DTR	Desired Threshold Range
MWIR	Mid-Wave Infrared
LWIR	Long-Wave Infrared
OVBC	Obviously Visible Background Clutters
IVBC	Invisible Background Clutters
ASD	Absolute Separation Degree
RSD	Relative Separation Degree

REFERENCES

- [1] C. L. Leonard, M. J. DeWeert, J. Gradie, J. Iokepa, and C. L. Stalder, "Performance of an EO/IR sensor system in marine search and rescue," in *Airborne Intelligence, Surveillance, Reconnaissance (ISR) Systems and Applications II*, Orlando, FL, United states, 2005, pp. 122-133.
- [2] B. Wang, L. Dong, M. Zhao, H. Wu, and W. Xu, "Texture orientation-based algorithm for detecting infrared maritime targets," *Applied optics*, vol. 54, no. 15, pp. 4689-4697, 2015.
- [3] X. Ran, and L. Ren, "Search aid system based on machine vision and its visual attention model for rescue target detection," in 2010 2nd WRI Global Congress on Intelligent Systems, Wuhan, China, 2010, pp. 149-152.
- [4] Z. Zhong, B. Zhang, G. Lu, Y. Zhao, and Y. Xu, "An Adaptive Background Modeling Method for Foreground Segmentation," *Intelligent Transportation Systems, IEEE Transactions on*, vol. 18, no. 5, pp. 1109-1121, Aug. 2016.
- [5] D. K. Prasad, D. Rajan, L. Rachmawati, E. Rajabally and C. Quek, "Video Processing From Electro-Optical Sensors for Object Detection and Tracking in a Maritime Environment: A Survey," *Intelligent Transportation Systems, IEEE Transactions on*, vol. 18, no. 8, Aug. 2017.
- [6] C. Li, H. Cheng, S. Hu, X. Liu, J. Tang and L. Lin, "Learning Collaborative Sparse Representation for Grayscale-Thermal Tracking," *Image Processing, IEEE Transactions on*, vol. 25, no. 12, pp. 5743-5756, Dec. 2016.
- [7] F. Wang, Y. Zhen, B. Zhong, and R. Ji, "Robust infrared target tracking based on particle filter with embedded saliency detection," *Information Sciences*, vol. 301, pp. 215-226, 2015.
- [8] N. Ikoma, and M. Koshiba, "Motion estimation of deformable target over infrared camera video in coarse resolution with possible frame-out of target by particle filter," in 10th Asian Control Conference (ASCC), Kota Kinabalu 2015, pp. 1-6.
- [9] Z. Li, J. Li, F. Ge, W. Shao, B. Liu, and G. Jin, "Dim Moving Target

- Tracking Algorithm Based on Particle Discriminative Sparse Representation," *Infrared Physics & Technology*, vol. 75, pp. 100-106, 2016.
- [10] N. Polson and V. Sokolov, "Bayesian Particle Tracking of Traffic Flows," *Intelligent Transportation Systems, IEEE Transactions on*, vol. 19, no. 2, pp. 345-356, Feb. 2018.
- [11] S. Kim, and J. Lee, "Small infrared target detection by region-adaptive clutter rejection for sea-based infrared search and track," *Sensors (Basel, Switzerland)*, vol. 14, no. 7, pp. 13210-13242, 2014.
- [12] X. Bai, and F. Zhou, "Analysis of new top-hat transformation and the application for infrared dim small target detection," *Pattern Recognition*, vol. 43, no. 6, pp. 2145-2156, 2010.
- [13] S. Panagopoulos, and J. J. Soraghan, "Small-target detection in sea clutter," *Geoscience and Remote Sensing, IEEE Transactions on*, vol. 42, no. 7, pp. 1355-1361, 2004.
- [14] B. Wang, W. Xu, M. Zhao, and H. Wu, "Antivibration pipeline-filtering algorithm for maritime small target detection," *Optical Engineering*, vol. 53, no. 11, pp. 113109, 2014.
- [15] J. Han, Y. Ma, B. Zhou, F. Fan, K. Liang, and Y. Fang, "A Robust Infrared Small Target Detection Algorithm Based on Human Visual System," *Geoscience and Remote Sensing Letters, IEEE*, vol. 11, no. 12, pp. 2168-2172, 2014.
- [16] J. Han, Y. Ma, J. Huang, X. Mei, and J. Ma, "An Infrared Small Target Detecting Algorithm Based on Human Visual System," *Geoscience and Remote Sensing Letters, IEEE*, vol. 13, no. 3, pp. 452-456, 2016.
- [17] Y. Lin, Y. Tong, Y. Cao, Y. Zhou and S. Wang, "Visual-Attention-Based Background Modeling for Detecting Infrequently Moving Objects," *Circuits and Systems for Video Technology, IEEE Transactions on*, vol. 27, no. 6, pp. 1208-1221, 2017.
- [18] Y. Chen, and Y. Xin, "An Efficient Infrared Small Target Detection Method Based on Visual Contrast Mechanism," *Geoscience and Remote Sensing Letters, IEEE*, vol. 13, no. 7, pp. 962-966, 2016.
- [19] S. Qi, D. Ming, J. Ma, X. Sun, and J. Tian, "Robust method for infrared small-target detection based on Boolean map visual theory," *Applied optics*, vol. 53, no. 18, pp. 3929-3940, 2014.
- [20] M. Nasiri, M. R. Mosavi and S. Mirzakuchaki, "IR small target detection based on human visual attention using pulsed discrete cosine transform," in *IET Image Processing*, vol. 11, no. 6, pp. 397-405, 6 2017.
- [21] B. Wang, L. Dong, M. Zhao, H. Wu, Y. Ji, and W. Xu, "An Infrared Maritime Target Detection Algorithm Applicable to Heavy Sea Fog," *Infrared Physics & Technology*, vol. 71, pp. 56-62, 2015.
- [22] F. A. Sadjadi, "Infrared target detection with probability density functions of wavelet transform subbands," *Applied optics*, vol. 43, no. 2, pp. 315-323, 2004.
- [23] C. C. Olson, K. P. Judd, K. Chander, A. J. Smith, M. Conant, and J. M. Nichols, "Watercraft detection in short-wave infrared imagery using a tailored wavelet basis," in Proc. SPIE 8391, Automatic Target Recognition XXII, 2012, pp. 83910K-1-11.
- [24] Y. Q. Sun, J. W. Tian, and J. Liu, "Background suppression based-on wavelet transformation to detect infrared target," in International Conference on Machine Learning and Cybernetics, USA, 2005, pp. 4611-4615.
- [25] D. Liu, L. Cao, Z. Li, T. Liu and P. Che, "Infrared Small Target Detection Based on Flux Density and Direction Diversity in Gradient Vector Field," in *IEEE Journal of Selected Topics in Applied Earth Observations and Remote Sensing*. Volume: PP, no. 99, pp. 1-27, May 2018.
- [26] X. Wang, Z. Peng, P. Zhang and Y. He, "Infrared Small Target Detection via Nonnegativity-Constrained Variational Mode Decomposition," in *IEEE Geoscience and Remote Sensing Letters*, vol. 14, no. 10, pp. 1700-1704, Oct. 2017.
- [27] Y. Chen, G. Y. Li, H. Wang, and T. Zhao, "Infrared Target Background Suppression Method Based on PDE and Morphological Filtering," *Applied Mechanics and Materials*, vol. 130-134, pp. 3686-3689, 2011.
- [28] F. Wang, and L. Quan, "Research of Thermal Infrared Target Detection by Second Prediction Difference Method and Top-Hat Transformation," *Applied Mechanics and Materials*, vol. 530-531, pp. 289-292, 2014.
- [29] B. Xie, L. Hu and W. Mu, "Background Suppression Based on Improved Top-Hat and Saliency Map Filtering for Infrared Ship Detection," *2017 International Conference on Computing Intelligence and Information System (CIIS)*, Nanjing, 2017, pp. 298-301.
- [30] H. Deng, X. Sun, M. Liu, C. Ye, and X. Zhou, "Small Infrared Target Detection Based on Weighted Local Difference Measure," *Geoscience and Remote Sensing, IEEE Transactions on*, vol. 54, no. 7, pp. 4204-4214, 2016.
- [31] D. D. Bloisi, F. Previtali, A. Pennisi, D. Nardi and M. Fiorini, "Enhancing Automatic Maritime Surveillance Systems With Visual Information," *Intelligent Transportation Systems, IEEE Transactions on*, vol. 18, no. 4, pp. 824-833, Apr. 2017.
- [32] X. Bai, Y. Bi, "Derivative Entropy-Based Contrast Measure for Infrared Small-Target Detection," *Geoscience and Remote Sensing, IEEE Transactions on*, vol. 56, no. 4, pp. 2452-2466, 2018.
- [33] Y. Shi, Y. Wei, H. Yao, D. Pan, G. Xiao, "High-Boost-Based Multiscale Local Contrast Measure for Infrared Small Target Detection," *IEEE Geoscience and Remote Sensing Letters*, vol. 15, no. 1, pp. 33-37, 2018.
- [34] M. Wan, G. Gu, W. Qian, K. Ren, and Q. Chen, "Robust infrared small target detection via non-negativity constraint-based sparse representation," *Applied optics*, vol. 55, no. 27, pp. 7604-7612, 2016.
- [35] C. Gao, D. Meng, Y. Yang, X. Zhou, and A. G. Hauptmann, "Infrared Patch-Image Model for Small Target Detection in a Single Image," *Image Processing, IEEE Transactions on*, vol. 22, no. 12, pp. 4996-5009, 2013.
- [36] C. Li, X. Sun, X. Wang, L. Zhang, and J. Tang, "Grayscale-Thermal Object Tracking via Multitask Laplacian Sparse Representation," *Systems, Man, and Cybernetics: Systems, IEEE Transactions on*, vol. 47, no. 4, pp. 673-681, 2017.
- [37] C. Gao, T. Zhang, and Q. Li, "Small infrared target detection using sparse ring representation," *Aerospace and Electronic Systems Magazine, IEEE*, vol. 27, no. 3, pp. 21-30, 2012.
- [38] B. Zhang, D. Jiao, H. Pei, Y. Gu, & Y. Liu, "Infrared moving object detection based on local saliency and sparse representation," *Infrared Physics & Technology*, vol. 86, pp. 187-193, Nov. 2017.
- [39] D. Liu, Z. Li, B. Liu, W. Chen, T. Liu, & L. Cao, "Infrared small target detection in heavy sky scene clutter based on sparse representation," *Infrared Physics & Technology*, vol. 85, pp. 13-31, Sep. 2017.
- [40] S. Kim, D. W. Yang and H. W. Park, "A Disparity-Based Adaptive Multihomography Method for Moving Target Detection Based on Global Motion Compensation," *Circuits and Systems for Video Technology, IEEE Transaction on*, vol. 26, no. 8, pp. 1407-1420, 2016.
- [41] C. L. P. Chen, H. Li, Y. Wei, T. Xia, and Y. Y. Tang, "A Local Contrast Method for Small Infrared Target Detection," *Geoscience and Remote Sensing, IEEE Transactions on*, vol. 52, no. 1, pp. 574-581, 2014.
- [42] J. Han, K. Liang, B. Zhou, X. Zhu, J. Zhao and L. Zhao, "Infrared Small Target Detection Utilizing the Multiscale Relative Local Contrast Measure," in *IEEE Geoscience and Remote Sensing Letters*, vol. 15, no. 4, pp. 612-616, April 2018.
- [43] C. Li, X. Wang, L. Zhang, J. Thang, H. Wu, L. Lin, "WELD: Weighted Low-rank Decomposition or Robust Grayscale-Thermal Foreground Detection," *Circuits and Systems for Video Technology, IEEE Transactions on*, vol. 27, no. 4, pp. 725-738, April 2017.
- [44] S. Yang, C. Li, G. Wang, J. Tang, "Fast Grayscale-Thermal Foreground Detection with Collaborative Low-Rank Decomposition," *Circuits and Systems for Video Technology, IEEE Transactions on*, vol. 28, no. 10, pp. 2574-2585, Oct. 2018.
- [45] C. Li, X. Liang, Y. Lu, N. Zhao, J. Tang, "RGB-T Object Tracking: Benchmark and Baseline," *Pattern Recognition*, vol. 96, pp. 106977, Dec 2019.
- [46] Y. Li, and Y. Zhang, "Robust infrared small target detection using local steering kernel reconstruction," *Pattern Recognition*, vol. 77, pp. 113-125, May 2018.
- [47] W. J. Plant, "Short wind waves on the ocean: Long-wave and wind-speed dependences," *Journal of Geophysical Research: Oceans*, vol. 120, no. 9, pp. 6436-6444, 2015.
- [48] N. Mayo, "Ocean waves—Their energy and power," *The Physics Teacher*, vol. 35, no. 6, pp. 352-356, 1997.
- [49] W. J. Pierson, and L. Moskowitz, "A proposed spectral form for fully developed wind seas based on the similarity theory of S. A. Kitaigorodskii," *Journal of Geophysical Research*, vol. 69, no. 24, pp. 5181-5190, 1964.
- [50] R. Keys, "Cubic convolution interpolation for digital image processing," *Acoustics, Speech and Signal Processing, IEEE Transactions on*, vol. 29, no. 6, pp. 1153-1160, 1981.
- [51] M. Sezgin, and B. I. Sankur, "Survey over image thresholding techniques and quantitative performance evaluation," *Journal of Electronic Imaging*, vol. 13, no. 1, pp. 146-168, 2004.
- [52] F. Yang, Q. Xu, B. Li, Y. Ji, "Ship Detection From Thermal Remote Sensing Imagery Through Region-Based Deep Forest," *IEEE Geoscience and Remote Sensing Letters*, vol. 15, no. 3, pp. 449-453, March 2018.



Bin Wang received the B.S. degree in Electronic Information Science and Technology, and the Ph.D. degree in Information and Communication Engineering from Dalian Maritime University, Dalian, China in 2013 and 2018, respectively. From 2016 to 2017, he was a joint Ph.D. candidate supervised by

Prof. Yuichi Motai at Virginia Commonwealth University, Richmond, VA, USA.

From 2015 to 2016, he finished the one-year study for Ph.D. candidate qualification at Dalian Maritime University, China. Since 2016, he continued his research at Virginia Commonwealth University, VA, USA as a joint Ph.D. candidate. This was sponsored by the China Scholarship Council. His research interests include infrared maritime image feature analysis and extraction, sea-surface target detection through digital image processing, maritime rescue and surveillance via infrared imaging, etc.



Emrah Benli (S'15, M'17) received the B.Sc. degree in Electronics and Communication Engineering from Kocaeli University, Kocaeli, Turkey, in 2009, the M.Sc. degree in Electrical Engineering from Clemson University, Clemson, SC, U.S.A., in 2013, and the Ph.D. degree in Electrical and Computer

Engineering from Virginia Commonwealth University, Richmond, VA, U.S.A. in 2017.

He was a Postdoctoral Fellow specializing in autonomous mobile robotics with the U.S. Army Research Laboratory's Computational and Information Sciences Directorate, Adelphi, MD, U.S.A., in 2018. He is currently an Academician of Electrical and Electronics Engineering at Gümüşhane University, Gümüşhane, Turkey. His research interests include intelligent systems, computer vision, artificial intelligence, multimodal sensory, robotic system design and control, and human-robot interaction.



Yuichi Motai (S'00–M'03–SM'12) received the B.Eng. degree in instrumentation engineering from Keio University, Tokyo, Japan, in 1991, the M.Eng. degree in applied systems science from Kyoto University, Kyoto, Japan, in 1993, and the Ph.D. degree in electrical and computer engineering from Purdue

University, West Lafayette, IN, U.S.A., in 2002. He is currently an Associate Professor of Electrical and Computer Engineering at Virginia Commonwealth University, Richmond, VA, U.S.A.

His research interests include the broad area of sensory intelligence; particularly in medical imaging, pattern recognition, computer vision, and sensory-based robotics.



Lili Dong was born in Qi Tai He City, Hei Long Jiang Province, China in 1980. She received the B.S. degree in Mechanical Design Manufacturing and Automation from Harbin Institute of Technology in 2002, the M.S. degree in Machine-Electronic Engineering from Harbin Institute of Technology in 2004, and the Ph.D. degree in Instrument Science and

Technology from Harbin Institute of Technology, in 2008.

From 2005 to 2008, she was a teaching assistant in the College of Information Science and Technology of Dalian Maritime University (DLMU). From 2008 to 2012, she was a lecturer in the College of Information Science and Technology of DLMU. Since 2012, she has been an assistant professor with the Mechanical Engineering Department. She is the author of 13 articles and 3 inventions. Her research interests include multispectral target recognition, tunnel lighting and photoelectric detection.



Wenhai Xu received his B.S. and M.S. degrees in Precision Instrument from Harbin Institute of Technology, Harbin, China in 1982 and 1984. He received his first Ph.D. degree in Precision Instrument from Harbin Institute of Technology in 1991. In 1993, he received his second Ph.D. degree in Manufacturing Machine from Tokyo Institute of Technology,

Tokyo, Japan.

From 1986 to 1988, he was a lecturer at Harbin Institute of Technology, Harbin, China. From 1992 to 2001, he was an assistant professor at the same university. He worked as the professor at Harbin Institute of Technology for 4 years since 2001. Meanwhile, he was hired as the project director at Cannon Inc., Tokyo, Japan from 1993 to 2003. He was also a research scientist at System Engineers' CO. LTD., Yamato City, Japan from 1995 to 1997. Now, he is a professor of Opt-Electric Information Science and Engineering at Dalian Maritime University, Dalian, China. In the last ten years, he has directed more than 30 research projects and applied 10 national patents. He is the author of more than 80 research papers. His research interests include infrared detection, digital image processing, design of high-resolution optical imaging system, opt-electronic information processing, etc.